Fourier analysis of an electrochemical phase formation model enables the rationalization of zinc-anode battery dynamics

Benedetto Bozzini [a], Maria Chiara D'Autilia [b], Claudio Mele [b], Ivonne Sgura [c,*]

[a] *Dipartimento di Energia, Politecnico di Milano, via Lambruschini, 4, Milano 20156, Italy*
[b] *Dipartimento di Ingegneria dell'Innovazione, Università del Salento, Via per Monteroni, Lecce 73100, Italy*
[c] *Dipartimento di Matematica e Fisica "E. De Giorgi", Università del Salento, Via per Arnesano, Lecce 73100, Italy*

ARTICLE INFO

ABSTRACT

The efficiency of safe, cheap and sustainable zinc-anode batteries is critically affected by the time-dependent formation of surface films that can impede the utilization of the active material. Knowledge regarding the nature and, in particular, the dynamics of these films is strongly wanting and both theoretical and experimental tools to rationalize the empirically observed behaviour are poorly developed. The present investigation concentrates on the electrode oscillating behaviour and presents an original experimental monitoring approach – based on the joint measurement of electrical and optical quantities - together with its physico-chemical modelling. The mathematical model considered is the DIB model of electrochemical phase formation, in its spatially homogeneous version: that is an ODE system coupling the dynamics of morphology and chemistry. The DIB parameters correspond to specific working conditions of the anode. Firstly, we analyse a Parameter Identification Problem (PIP) based on Fourier regularization. Secondly, a specific PIP is proposed for relaxation oscillations, based on the analysis of the geometry of the limit cycle. The results of this work allow a notable step forward in the understanding on zinc-anode instabilities and open up the perspective of closed-loop control of anode activity state, in view of battery control, also exploiting the higher sensitivity enabled by jointly transducing electrical and optical quantities.

1. Introduction

The constantly growing demand of electrical energy calls for replacement of production with fossil fuels with sustainable technologies, primarily renewable sources, that are intermittent in nature and thus require reliable and, again, sustainable storage facilities of appropriate capacity and power. At this moment, electrochemical energy storage (EES) based on batteries seems the only viable approach for the near future, but devices for real-life applications still have to be brought to the marketable level. Moreover, safe and environmentally friendly EES chemistries have to be developed and implemented. Among well-developed battery technologies, those based on lead, nickel-cadmium, lithium and hydrogen can in principle can be employed for large-scale EES, but they exhibit notable criticalities in terms of cost, durability and safety. Systems at a lower technology readiness level, that have demonstrated promising performance at the pilot scale, are redox-flow and zebra batteries, that nevertheless still exhibit criticalities related to the materials employed, as well as complexities in the scale-up for real-life storage requirements. In this scenario, zinc-based technologies, though still scarcely developed in large-scale applications, exhibit probably the highest prospect in terms of sustainability, ease of sourcing, intrinsic safety and cost-effectiveness. Technologies based on zinc-anodes can be combined with a variety of green cathodic chemistries, including air reduction and ion intercalation, and can be built in sealed, flow, electrically and mechanically rechargeable versions. The high appeal of zinc as an anodic material is currently in part jeopardized by the complexity of its behaviour in battery ambient. Even if this material has been employed successfully in many low-power applications, starting from Volta's first demonstration of a battery in 1799, it still displays several surprising aspects, especially dynamic ones, that limit its use in high-power devices. These peculiarties involve the reactions going on both during battery discharge and charge. In brief, metal in many aqueous ambients exhibits a passivating behaviour, that essentially means that when it reacts in the process corresponding to discharge, it generates reaction products that tend to stop the reaction itself. The electrical counterpart of this chemical behaviour, is that the system exhibits a negative resistance (see Fig. 1), that, in turn, opens up a range of electrical instability scenarios, typically giving rise to oscillating behaviour (Bozzini et al., 1999). During recharge, instead, zinc tends to change
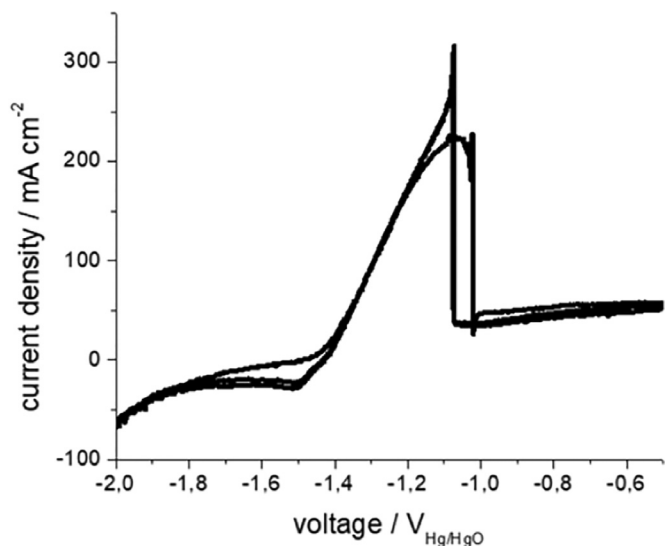
Fig. 1. Current-voltage curves, obtained by linear-sweep voltammetry at 1 mV s^{-1}, for a Zn electrode in contact with a 6 M KOH aqueous solution.

its geometry, forming odd-shaped objects (see Figure 2) that eventually lead to metal crumbling, causing battery capacity loss, and to internal short-circuits (Rossi et al., 2020).

In this paper, we concentrate on some dynamic aspects related to zinc behaviour during battery discharge, that are connected to the termination of current delivery, still in the presence of even notable fractions of residual active material, of course causing energetic inefficiency: more information on these problems, at the materials-science level, can be found in the following recent publications (Blanc et al., 2020; Rossi et al., 2020; Shin et al., 2020; Yu et al., 2020). Specifically, we shall study the response of zinc-anodes in the typical battery electrolyte consisting of an alkaline aqueous solution, by electrical and optical methods, detailed below. Electrochemical measurements show a variery of dynamic scenarios, that have been preliminarity presented in Bozzini et al. (2019) and will form the object of a dedicated publication. In this work we focus our interest on the special case of oscillatory behaviour, as followed by current oscillations resulting from the application of a constant potential, recorded simultaneously with reflectivity oscillations. It is worth noting that the time-dependence of optical reflectivity is highly diagnostic of the formation of passivating films at the zinc-electrolyte interface and, in principle, enables monitoring of the battery state-of-health and early detection of potentially critical operating regimes. This is the first systematic analysis of coupled electrical-

optical dynamics in electrochemical systems, after their phenomenological presentation in Bozzini et al. (2019).

Space-time dynamic processes of zinc-anodes can be rationalized in the framework of the DIB electrochemical phase-formation model that we have been developing over the last decade (Bozzini et al., 2018; 2013; Lacitignola et al., 2015; 2018; 2019). In the specific case of global electrodic oscillations, an ODE version of the DIB model can be formulated, in which the two equations describe the dynamics of the morphology of the electrode surface and its degree of coverage with a passivating film. The source terms in the model contain simple physico-chemical information on electrokinetics and electrochemically-driven adsorption, formulated in terms of phenomenological reaction rates. In particular, we could follow the oscillating regimes of the two unknowns, that correlate to the current and reflectivity oscillations observed experimentally reproducing the key details of the dynamic structure of the process and identifying the physical parameters of the model. The dynamics of the zinc electrode impacts the time-dependent behaviour of a battery both during discharge (in which oscillations are characteristic of aged devices (Arai, 2015)) and charge (owing to the presence of an autocatalytic step in the zinc plating process (Lacitignola et al., 2017; Zhu et al., 2016)). Electrical battery instability during discharge corresponds to working conditions in the bistable zone of the current-voltage characteristic curve (Figure 1) and anticipates the attainment of the cut-off voltage (see, e.g. Masri and Mohamad, 2013). Oscillatory behaviour during recharge can instead be explained with the establishment of localization processes during zinc plating onto electrodes that exhibit a distribution of passivated and active areas (Rossi et al., 2020).

In Section 2, we present our experimental results. In Section 3, we present a Fourier analysis, based on the DIB model, of an experimental current density time series corresponding to the morphological solution of the DIB model. Specifically, we study a Parameter Identification Problem (PIP) based on the Fourier regularization method introduced in D'Autilia et al. (2017) for modelling oscillating electrochemical data. This approach avoids the ill-posedness of the usual least-squares cost functions, and is able to find an iso-frequency manifold in the parameter space, where target oscillatory data and simulations have the same frequency, such that along this manifold the dephasing can be minimized. In Section 4, the DIB model is used again in a PIP problem, but here based on the specific time-profile of the same set of experimental relaxation oscillations. Since the experimental oscillations are of the relaxation type, we studied the curvature of the limit cycle of the DIB model and identified a parameter subregion where an inflexion point is present, corresponding to the peculiar class of experimental waveforms. Finally, in Section 5, the approaches described in Sections 3 and 4 are employed jointly for the analysis of current density and reflectivity time series, corresponding to the two DIB model solutions: morphological and chemical, respectively.
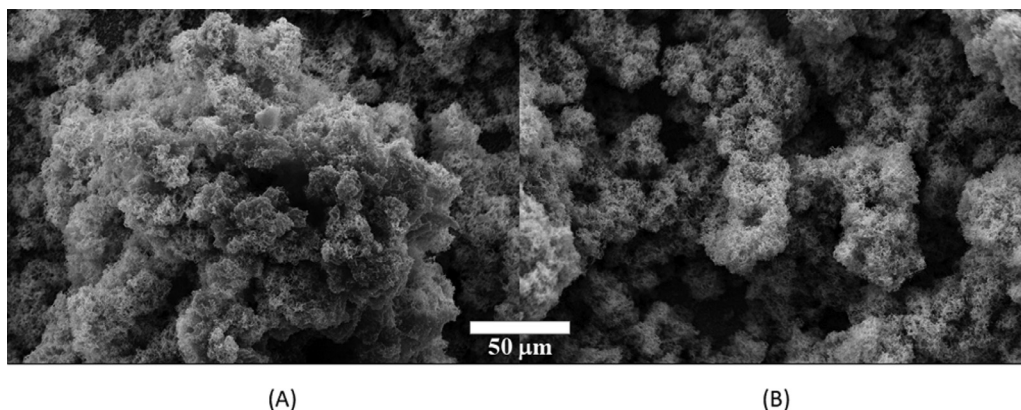

Fig. 2. Scanning electron micrographs of typical unstable Zn growth morphologies. Electrodeposits obtained by galvanostatic plating at 10 mA cm^{-2} for 1 h (A) no additive, (B) benzyl-phenyl modified polyethyleneimine (BBPEI) 0.1 g L^{-1}.
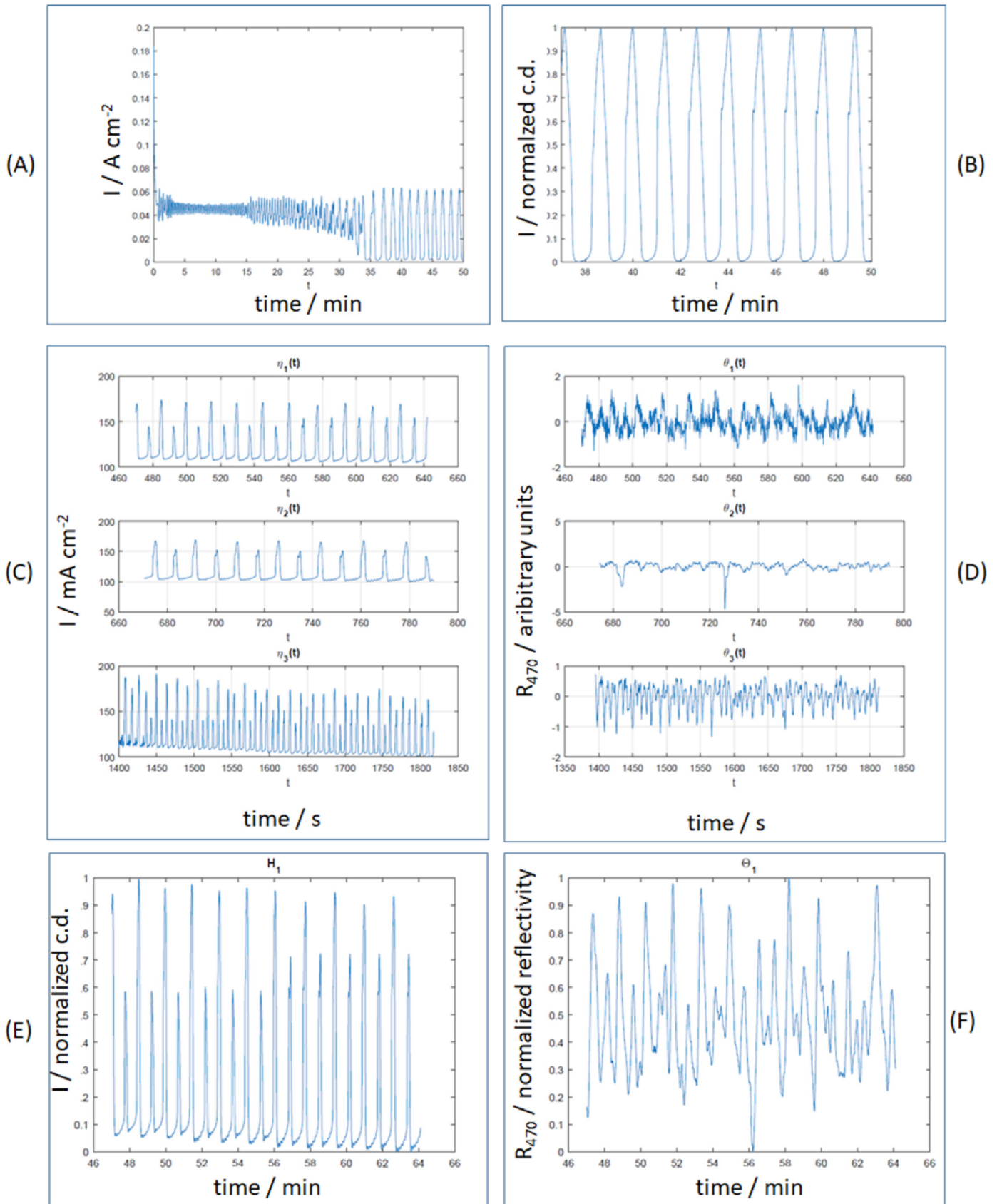
Fig. 3. The three experimental time-series studied in this work, obtained with Zn electrode in contact with a 6 M KOH aqueous solution. (A, B) Current density (c.d.) (I) time series, obtained by potentiostatic polarization at -1012 mV$_{Hg/HgO}$: (A) the whole recorded time-series; (B) the quasi-steady oscillation interval analysed, after trend removal and normalization. (C) Current density (I) and (D) reflectivity at 470 nm (R$_{470}$), obtained by potentiostatic polarization at -1020 mV$_{Hg/HgO}$. (E, F) The quasi-steady oscillation intervals of I and R$_{470}$ analysed, after trend removal and normalization.

2. Materials and experimental methods

As working electrode, we employed the freshly-polished cross-section of a high-purity (99.99 + %, Goodfellows) zinc (Zn) rod (7.6 mm in diameter). Polishing was performed before each measurement with grit papers down to 2500. The electrolyte was a 6M KOH aqueous solution, prepared with Milli-Q water. The reference electrode was Hg/HgO and the counter electrode a high-area Pt wire. Combined electrochemical and electroreflectance measurements were performed with a VersaSTAT 3F potentiostat, operated potentiostatically in the floating mode, measuring current density (indicated by I) time series. In situ electroreflectance was carried out with a self-constructed spectrometer, described in Bozzini et al. (2008). With the chemistry of interest, in situ reflectivity measurements, responsive to the formation of passivation films, can be carried out in the whole VIS-UV spectral range, but, on the basis of our results reported in Mele and Bozzini (2015), to record reflectivity time-series, we selected the VIS wavelength 470 nm, that is particularly sensitive to the metal-oxide transition. In fact, even if reflectivity at this wavelength is relatively low, though measurable with a good signal-to-noise ratio, for metallic Zn, it is notably higher for ZnO, thus yielding a high chemical contrast, compatible with the dynamic range of the detector. Thus, increases of reflectivity at 470 nm (indicated by R_{470}) correspond to the formation of ZnO films and decreases to their dissolution, yielding a high surface fraction of metallic Zn. Long-term decreasing trends correspond to progressive electrode roughening, that accompanies the anodic process. In this study, we concentrate on the analysis of three representative experimental time-series, shown in Fig. 3, one of I recorded at –1012 mV$_{Hg/HgO}$ and two of I and R$_{470}$, measured simultaneously by applying –1020 mV$_{Hg/HgO}$. As expected, the oscillating behaviour occurs in the potential range where the current-voltage curve exhibits the characteristic S-shape, corresponding to the active-passive transition. According to our discussion in Bozzini et al. (2019) and Mele et al. (2017), the oscillations considered in this work are of the self-sustained relaxation type, and correspond to the formation of a compact, passivating type of zinc oxide.

Numerical method: In the next sections, we will solve the parameter identification problem (PIP) as a constrained optimization problem, where the constraint is the DIB model given as an ODE system with oscillating solutions. To obtain the cost function in the parameter space based on the Fourier analysis, we need to solve numerically several times the ODE system for different choices of the parameters involved. To this aim, as in D'Autilia et al. (2017), we will apply the explicit Runge-Kutta method of order four (RK4) that has good properties to minimize the numerical dispersion when applied for tracking oscillating solutions (see the analysis in the Appendix of D'Autilia et al. (2017)). All numerical computations here presented have been implemented in the Matlab environment (MATLAB, 2019).

3. DIB Parameter Identification for oscillating current-density time series, based on Fourier analysis

We consider the DIB-PIP minimization problem defined as:

$$\min_{(C,B)\in\Omega} J(\eta(t), \widetilde{\eta}(t), C, B) \tag{1}$$

where $\eta(t)$ is solution of

$$\begin{cases} \eta'(t) = f(\eta, \theta), & t \in]0, T] \\ \theta'(t) = g(\eta, \theta) \\ \eta(0) = \eta_0, \ \theta(0) = \theta_0, \end{cases} \tag{2}$$

and where the kinetics are given by:

$$f(\eta, \theta) = A_1(1-\theta)\eta - A_2\eta^3 - B(\theta - \alpha), \tag{3}$$

$$g(\eta, \theta) = C(1 + k_2\eta)(1-\theta)(1-\gamma(1-\theta)) - D(\theta(1-\gamma\theta) + k_3\eta\theta(1 + \gamma\theta)). \tag{4}$$

These nonlinear source terms are the same as in the spatially dependent DIB PDE model introduced in Bozzini et al. (2013) and Lacitignola et al. (2015) and they account for generation (deposition) and loss (corrosion) of the relevant material during the electrodeposition process. For aim of completeness, we briefly report here the meaning of the kinetics (3) and (4), full details are provided in Bozzini et al. (2013) and Lacitignola et al. (2015). In the kinetics (3), the term $A_1(1-\theta)\eta$ accounts for the charge-transfer rate at sites free from adsorbates; $A_2\eta^3$ describes mass-transport limitations to the electrodeposition process. The term $-B(\theta - \alpha)$ quantifies the effect of adsorbates on the electrodeposition rate. The parameter $0 < \alpha < 1$ takes into account the fact that adsorbates can have both inhibiting and enhancing effects on the growth rate. The kinetics (4) can be regarded as $g(\eta, \theta) = Cg_{ads}(\eta, \theta) - Dg_{des}(\eta, \theta)$ and features adsorption (parameter C) and desorption (parameter D) terms including both chemical (expanded to second order) and electrochemical (first order) contributions.

In this paper, as in Lacitignola et al. (2015), we fix the following parameter values $\alpha = 0.5$, $\gamma = 0.2$, $k_2 = 2.5$, $k_3 = 1.5$, $A_1 = 10$, $A_2 = 30$ and we consider the Hopf and the transcritical bifurcation lines in the parameter space (C, B) identified by the bifurcation points TH and TB of coordinates $(C_{TH}, B_{TH}) = (2.8061, 109.13)$, $(C_{TB}, B_{TB}) = (2.8061, 19.7979)$, respectively. According to the analysis in Lacitignola et al. (2015), the equilibrium $P_e = (\eta_e, \theta_e) = (0, \alpha)$ (such that $f(0, \alpha) = g(0, \alpha) = 0$) is unstable in the region on the left of the Hopf line and above the transcritical one and we expect homogeneous oscillations due to the presence of a stable limit cycle, caused by a supercritical Hopf bifurcation. For this reason, for our application to oscillatory data, in the minimization problem (1) we search the optimal parameters (C, B) in the domain $\Omega = [C_i, C_f] \times [B_i, B_f] = [0, 2.8] \times [21, 100]$.

To solve the minimization problem (1) and (2) the "classical" direct approach uses the 2-norm:

$$J_{norm2}(C, B) = \|H(C, B) - \widetilde{H}_{exp}\|_2^2 \tag{5}$$

where $H(C, B) = [H_0, ..., H_N] \in \mathbb{R}^{N+1}$ is the numerical approximation of $\eta(t)$ in (2) with a timestep $h = \frac{T - t_0}{N}$, that is $H_0 = \eta_0$ and $H_k \approx \eta(t_k)$, for $k = 1, .., N$ on $t_k = t_0 + k h$. $\widetilde{H}_{exp}$ is the vector of the target data. Here we consider $\widetilde{H}_{exp}$ as original experimental data, given by the values $\widetilde{H}_{exp} = [\widetilde{H}_0, ..., \widetilde{H}_{\widetilde{N}}] \in \mathbb{R}^{\widetilde{N}+1}$ on the time interval $t \in [0, T] = [0, 50]$ obtained every timestep $h_{exp} = 0.01$.

In our DIB-PIP we shall neglect the transient dynamics and focus only on the asymptotic oscillatory behaviour of current-density data, after normalization, for $t \in [t_1, T] = [t_1, 50]$, where t_1 is specific of a given experimental data-chunk. To this aim, we obtain $H(C, B)$, the numerical solutions of the DIB-ODE system, by RK4 with timestep $h = 0.005$, $\eta_0 = 0.1$ and $\theta_0 = 0.2$. We then extract the solution in the interval $t \in [t_1, 50]$ and normalize it. For comparison of experimental and computed data, the former are interpolated on the ODE grid. For notational convenience, we still call $H(C, B)$ and $\widetilde{H}_{exp}$ these reduced vectors.

In the present section, we shall apply the Fourier regularization approach proposed in D'Autilia et al. (2017). The dominant frequencies $\widetilde{f}_1, \widetilde{f}_2, ...$ are identified by computing the FFT with the Matlab function fft, whence the Fourier cost for the first harmonic was defined as:

$$J_{FFT}^1(C, B) = \frac{|f_1(C, B) - \widetilde{f}_1|}{\widetilde{f}_1}, \tag{6}$$

where $f_1(C, B)$ is the first dominant frequency of $H(C, B)$ for all $(C, B) \in \Omega_h$. The set Ω_h is obtained by discretizing the search domain Ω defined before by using the stepsizes $h_C = 0.025$ and $h_B = 0.25$. We can identify the pairs (C, B) for which $J_{FFT}^1(C, B) = 0$, and store them in the set $\Omega_{FFT}^1 \subset \Omega_h$, such that

$$\Omega_{FFT}^1 = \{(C_i, B_j) \in \Omega_h \mid J_{FFT}^1(C_i, B_j) = 0\}. \tag{7}$$

In principle, it is also possible to consider the cost functions for n higher harmonics and construct the corresponding Ω_{FFT}^n sets recursively, as

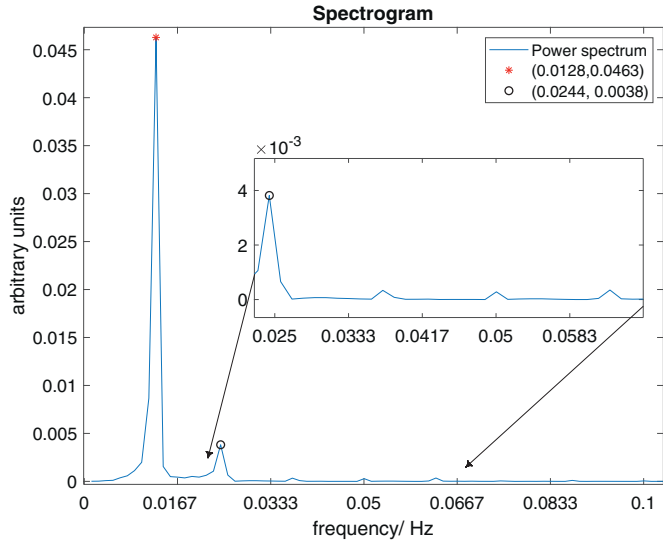**Fig. 4.** The power spectrum of the experimental data-chunk $\widetilde{H}_{exp}^1$, shown in Fig. 3-B.

follows. By defining

$$J_{FFT}^2(C, B) = \frac{|f_2(C, B) - \widetilde{f}_2|}{\widetilde{f}_2}, \tag{8}$$

where $f_2(C, B)$ is the second dominant frequency of $H(C, B)$ for all $(C, B) \in \Omega_{FFT}^1$, we construct the set Ω_{FFT}^2 as

$$\Omega_{FFT}^2 = \{(C_i, B_j) \in \Omega_{FFT}^1 \mid J_{FFT}^2(C_i, B_j) = 0\}, \tag{9}$$

and so on. This approach would be specially rewarding to follow oscillations of the harmonic type, but its application to the case of relaxation oscillations would require an impractical number of components. It can be shown that the relaxation oscillations of our experimental dataset would require at least twelve Fourier components, to follow adequately the observed waveform. Here we employed the first-order Fourier method for the analysis of the oscillatory data-chunk depicted

in Fig. 3-B and corresponding to the interval $t \in [37s, 50s]$ of the more complex time-series shown in Fig. 3-A and we show that an incremental improvement can be obtained by considering also the second harmonic. The power spectrum of the analysed dataset is reported in Fig. 4, with indication of the first and second dominant frequencies.

As a first step in our analysis, we follow the approach of D'Autilia et al. (2017) and apply the Fourier regularization to identify in the (C,B) plane the pairs of parameters such that the numerical simulations exhibit the same dominant frequency as the experimental data. We thus compute the Fourier cost $J_{FFT}^1(C, B)$ in (6), shown in Fig. 5-A, for the pairs $(C, B) \in \Omega_h$, whence we identify the set Ω_{FFT}^1, depicted in Fig. 5-B. Once Ω_{FFT}^1 is available, it is possible to evelute a given cost function, limiting the optimum search to this subset of the (C,B) plane. Specifically, we have tested four cost functions defined below: the infinity norm (10), the least-squares norm (11) and the time-lag norms (12) and (13). The time-lag norms, that we have evaluated with respect to the first (12) and last (13) point in the time-series, allow to minimize the dephasing of the normalized chunks of quasi-periodic data. For $C \in [C_i, C_f]$, we define:

$$J_\infty^{\Omega_{FFT}^1}(C) = J_\infty(C, B)\big|_{\Omega_{FFT}^1} = \|H(C, B) - \widetilde{H}_{exp}^1\|_\infty, \tag{10}$$

$$J_2^{\Omega_{FFT}^1}(C) = J_{2norm}(C, B)\big|_{\Omega_{FFT}^1} = \|H(C, B) - \widetilde{H}_{exp}^1\|_2^2, \tag{11}$$

$$J_{TL}(C) = J_{TimeLag}(C, B)\big|_{\Omega_{FFT}^1} = |H_1(C, B) - (\widetilde{H}_{exp})_1^1|, \tag{12}$$

$$J_{TLE}(C) = J_{TimeLagEnd}(C, B)\big|_{\Omega_{FFT}^1}$$
$$= |H_N(C, B) - (\widetilde{H}_{exp})_N^1|, \tag{13}$$

Fig. 6 reports the evaluation of the four norms (10)–(13) along the manifold of Fig. 5-B. Their minima are found in the following sets of points: $(C_{10}, B_{10}) = (0.575, 96.5), (C_{11}, B_{11}) = (0.6, 92.5), (C_{12}, B_{12}) = (1.4, 52.5), (C_{13}, B_{13}) = (2.15, 41.5)$. The numerical simulations corresponding to these minima are shown in Fig. 7, together with the corresponding absolute errors.

Computing the cost for the second harmonic J_{FFT}^2 defined in (8) for the (C,B) pairs contained in Ω_{FFT}^1, and searching the pairs that satisfy
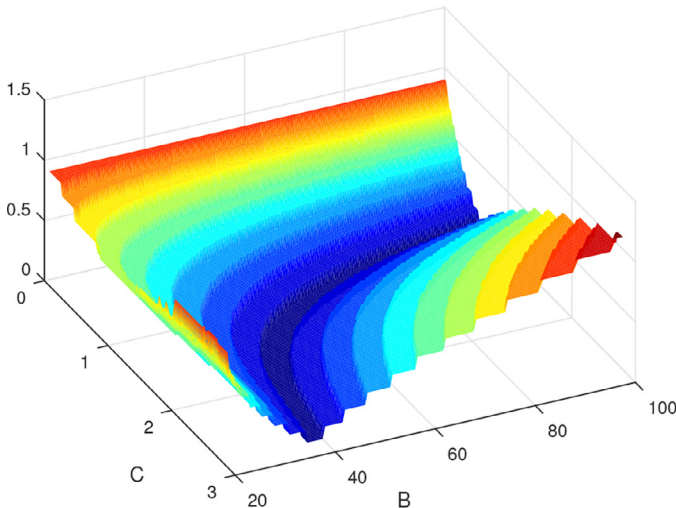
(A)
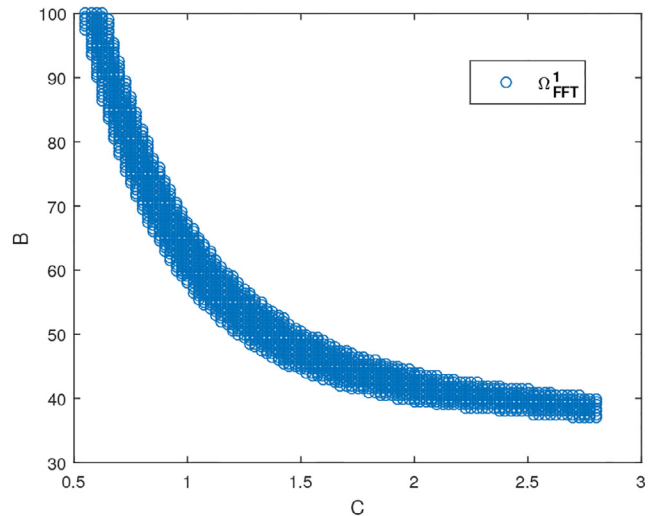
(B)

Fig. 5. (A) The cost function of the first harmonic $J_{FFT}^1(B, C)$ in (6) and (B) the set Ω_{FFT}^1 in (7), computed for the dataset of Fig. 3-B.
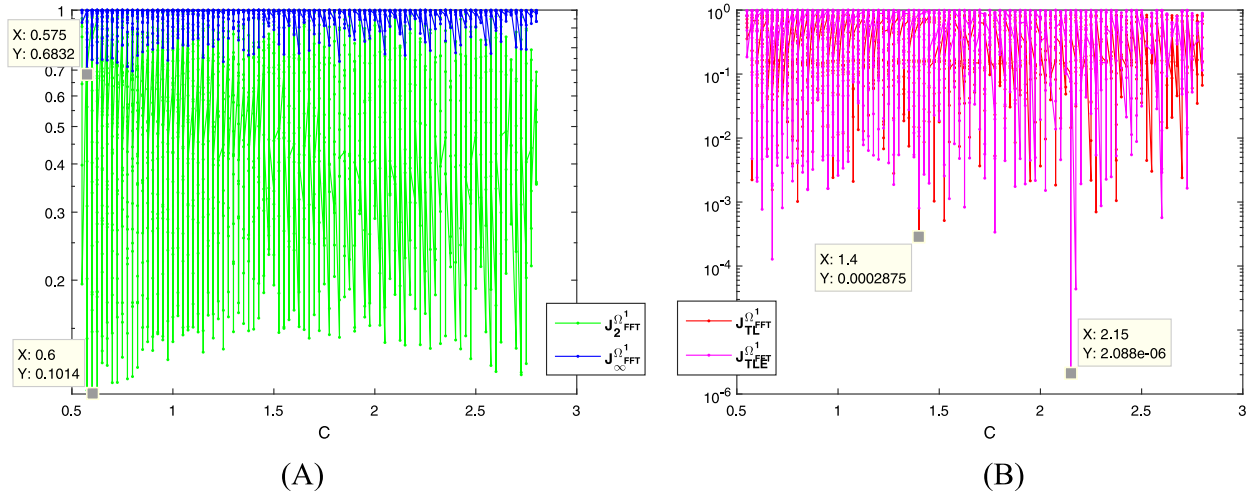
Fig. 6. Cost functions (10)–(13) evaluated on the subset of the parameter space Ω^1_{FFT} in Fig. 5B for the dataset of Fig. 3-B. (A) Cost functions (10) and (11); (B) cost functions (12) and (13).
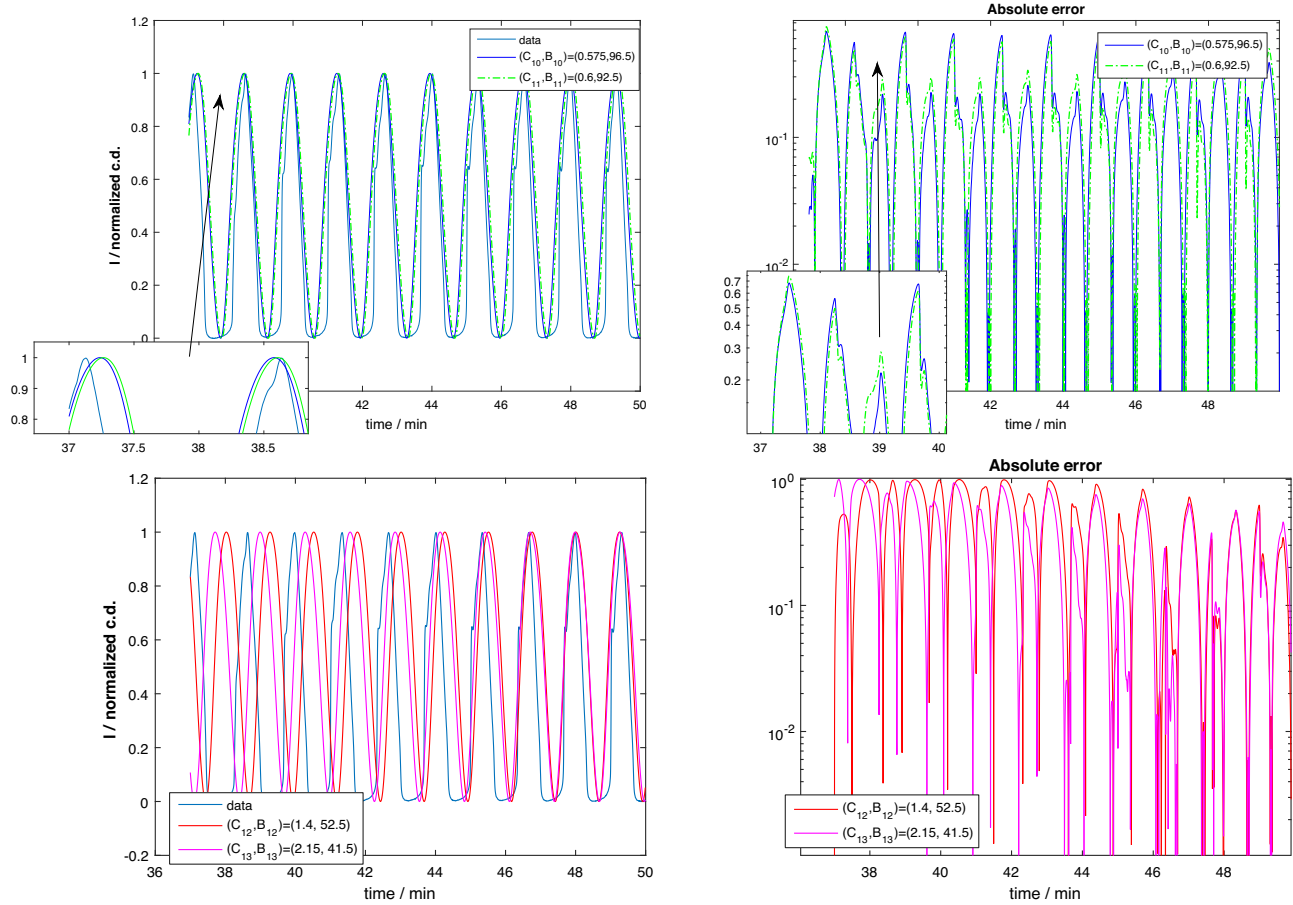

Fig. 7. Comparison of experimental data and numerical simulations obtained with (C,B) values set at the minima of $J^{\Omega^1_{FFT}}_\infty$ (C_{10}, B_{10}), $J^{\Omega^1_{FFT}}_2$ (C_{11}, B_{11}) (top panels) J_{TL} (C_{12}, B_{12}), J_{TLE}(C_{13}, B_{13}) (bottom panels). The corresponding absolute errors are reported in the panels on the right.

the condition $J^2_{FFT}(C, B) = 0$, the set Ω^2_{FFT} defined in (9) can be derived (Fig. 8-A). Optimum search has been performed over Ω^2_{FFT}, minimizing the following infinity norm (see Fig. 8-B):

$$J^{\Omega^2_{FFT}}_\infty(C) = J_\infty(C, B)_{|_{\Omega^2_{FFT}}} = \|H(C, B) - \widetilde{H}^1_{exp}\|_\infty, \quad C \in [C_i, C_f], \quad (14)$$

yielding the optimal couple (C_{14}, B_{14}) = $(1.25, 50)$. Inclusion of second-harmonic information, as expected in the case of relaxation oscillations, cannot improve markedly the identification of the waveform, but nevertheless it allows a more precise approximation of the sharp maxima (Fig. 9-A) and the selection of a solution of the DIB model that also contains the second Fourier component (Fig. 9-B). Fourier-based PIP thus
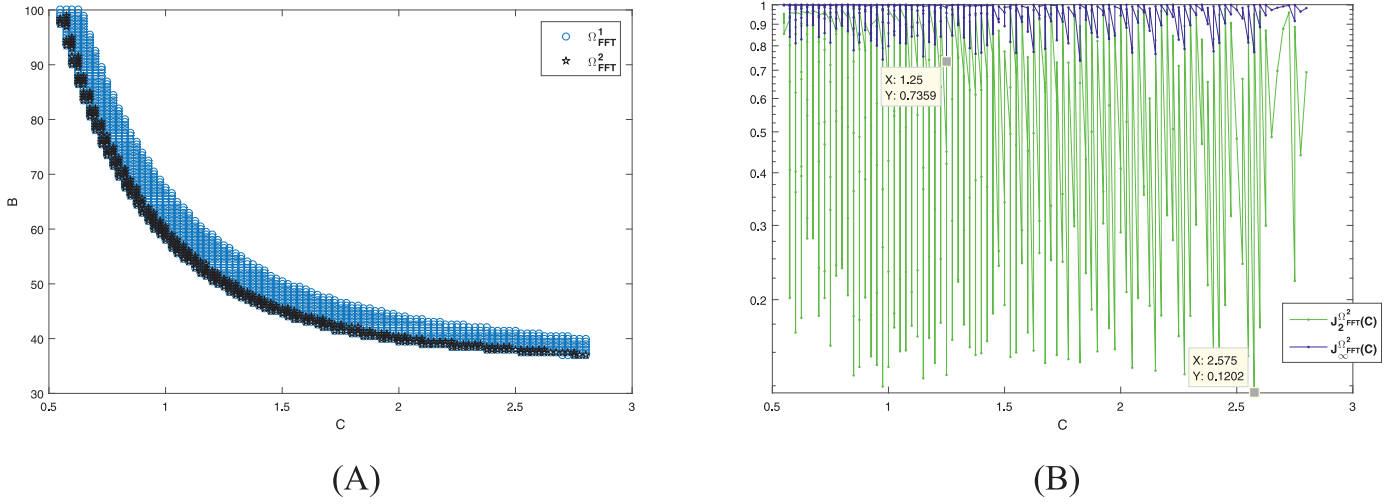
Fig. 8. (A) The sets Ω_{FFT}^1 and Ω_{FFT}^2 of the parameter space, and (B) the cost functions (14) and (15) evaluated on Ω_{FFT}^2 for the dataset of Fig. 3-B.
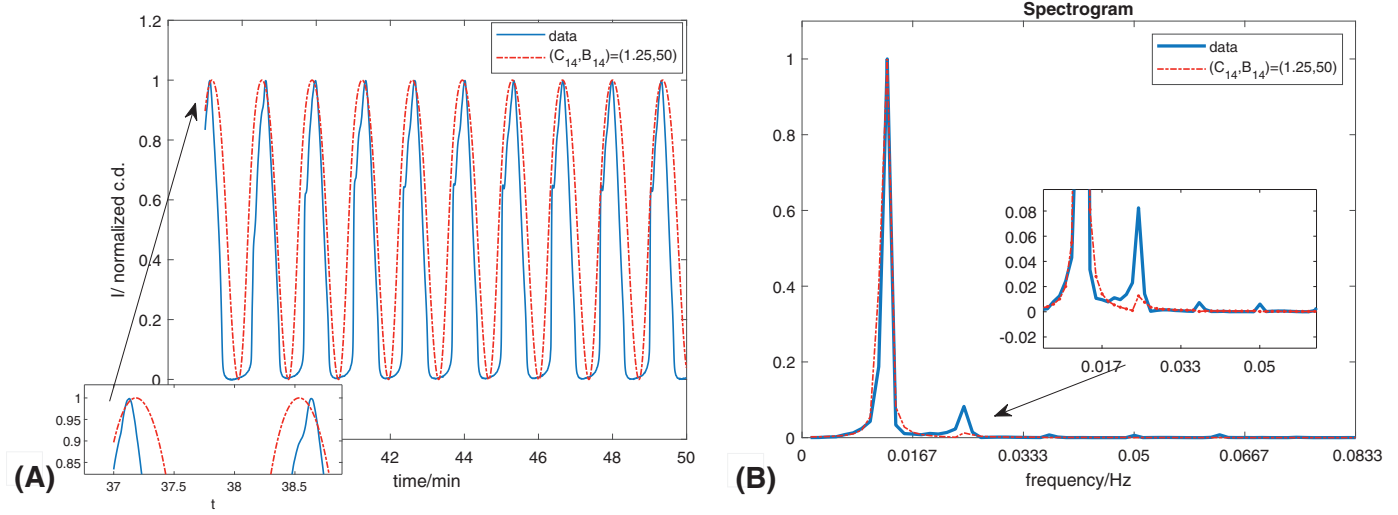

Fig. 9. (A) Comparison of experimental and numerical simulations obtained with (C,B) values set at the minimum (C_{14}, B_{14}). (B) Comparison of the power spectral densities for experimental and numerical simulations obtained with (C,B) values set at the minimum (C_{14}, B_{14}).

allows to identify accurately the DIB solution exhibiting the main frequency components, thus capturing important aspects of the system dynamics. Nevertheless, a different strategy, presented in the next section, is necessary to approximate precisely also the details of the waveform.

4. DIB Parameter Identification for relaxation current-density oscillations, based on limit cycle analysis

4.1. Identification of the relaxation oscillation region in the parameter space

Relaxation oscillations are characterized by a limit cycle that changes its concavity: based on this property, it is possible to restrict optimum search in the subset of the parameter space that corresponds to this particular type of dynamic behaviour. For this purpose, let $\alpha(t)$ be the parametric equation of the limit cycle, a curve in the $\eta - \theta$ plane:

$$\alpha(t) = (\eta(t), \theta(t)), \quad t \geq 0. \tag{15}$$

The algebraic curvature is defined as follows:

$$\mathcal{K}(t) = \frac{\eta'(t)\theta''(t) - \eta''(t)\theta'(t)}{(\sqrt{\eta'(t)^2 + \theta'(t)^2})^3} \tag{16}$$

and it yields information about the direction of rotation of the tangent, negative and positive values corresponding to clockwise and anticlockwise rotation, respectively. A change in sign of $\mathcal{K}(t)$ denotes an inflection point. The first order derivatives in (16) can be obtained by the DIB kinetics $f(\eta, \theta)$ in (3) and $g(\eta, \theta)$ in (4). The second order derivatives appearing in (16) can be calculated by the DIB kinetics as follows:

$$\begin{cases} \eta'' = A_1(-\theta')\eta + A_1(1-\theta)\eta' - 3A_2\eta^2\eta' - B(\theta') \\ \theta'' = C(1+k_2\eta')(1-\theta)(1-\gamma(1-\theta)) + C(1+k_2\eta)(-\theta')(1-\gamma(1-\theta)) \\ +C(1+k_2\eta)(1-\theta)(\gamma\theta') + \\ -D[\theta'(1+\gamma\theta)+\theta(\gamma\theta')+k_3\eta'\theta(1+\gamma\theta)+k_3\eta\theta'(1+\gamma\theta)+k_3\eta\theta(\gamma\theta')]. \end{cases} \tag{17}$$

Of course, explicit expressions for $\eta(t)$ and $\theta(t)$ are not available, but they can be obtained numerically. Let $H(C, B) = [H_0, ..., H_N]$, $\Theta(C, B) = [\Theta_0, ..., \Theta_N] \in \mathbb{R}^{N+1}$ be the numerical approximations of $\eta(t)$ and $\theta(t)$ with a timestep $h = \frac{T-t_0}{N}$ for $(C, B) \in \Omega_h$ and all the other parameters fixed as in Section 2. Thus we can compute the vectors $H'(C, B)$, $\Theta'(C, B)$, $H''(C, B)$ and $\Theta''(C, B)$ as the approximations of η', θ', η'' and θ'' respectively, from the analytic expressions in (3)-(4)-(17). Then, we
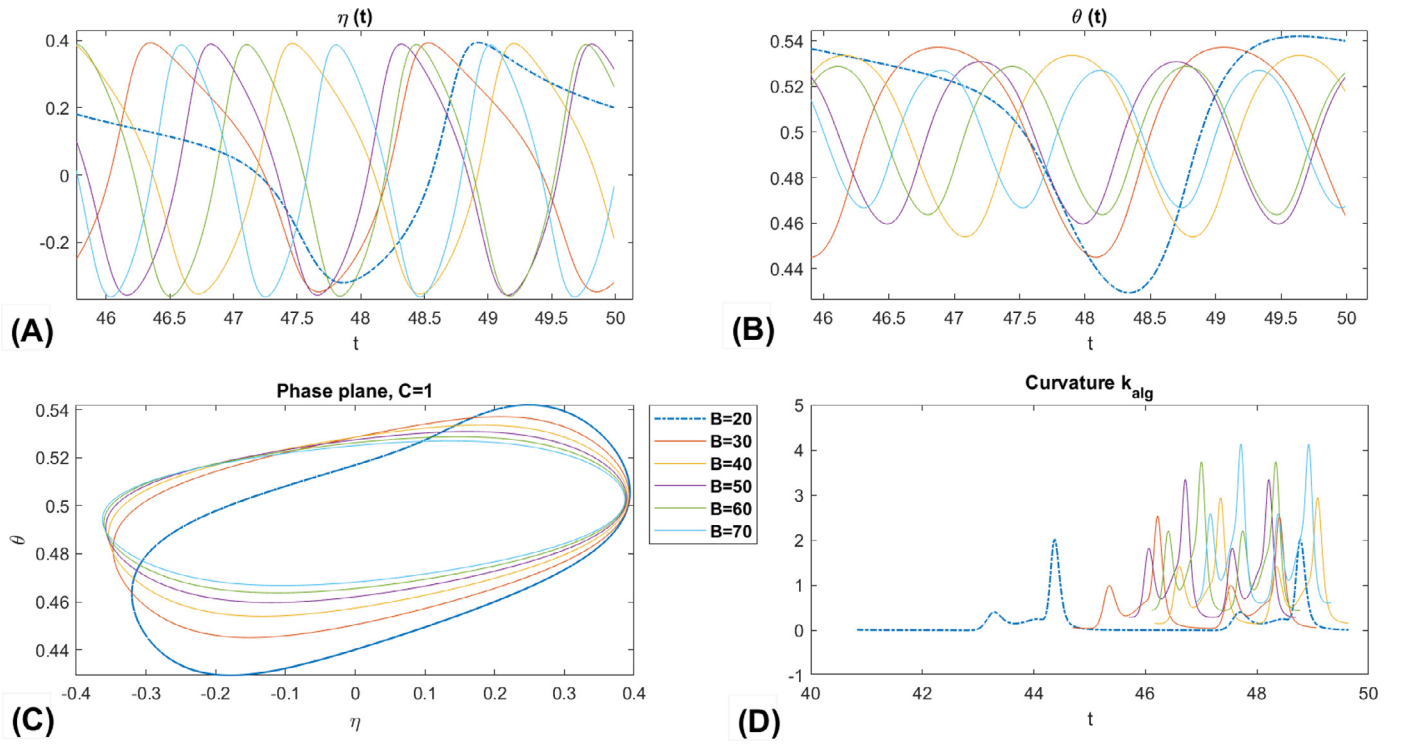
Fig. 10. Case $C = 1$ and $B \in [20, 70]$. (A, B) Representative solutions of the DIB model $\eta(t), \theta(t)$, reported for $t \in [46, 50]$. (C) Limit cycles for the solutions reported in Panels (A, B). (D) Algebraic curvature of the limit cycles shown in Panel (C). Data corresponding to the solutions yielding a limit cycle with an inflection point are plotted with a dashed line.

can restate (16) as:

$$\mathcal{K}(C, B) = \frac{H'(C, B)\Theta''(C, B) - H''(C, B)\Theta'(C, B)}{\left(\sqrt{H'^2(C, B) + \Theta'^2(C, B)}\right)^3}. \tag{18}$$

A representative selection of waveforms and corresponding limit cycles, obtained by varying $B \in [20, 70]$, keeping $C = 1$, is shown in Fig. 10: here the transition from quasi-harmonic to relaxation oscillations can be readily noted. Here $H(C, B)$ and $\Theta(C, B)$ have been computed using the well-known Runge-Kutta4 with timestep, $h = 0.005$. With these tools, we proceed to identify the set $\Omega_{\mathcal{K}}$ of (C, B) pairs such that $\mathcal{K}(C, B)$ exhibits an inflection point, diagnostic of relaxation oscillations, by computing (18) for all $(C, B) \in \Omega_h$:

$$\Omega_{\mathcal{K}} = \{(C_i, B_j) \in \Omega_h \mid \mathcal{K}(C_i, B_j) \text{ has an inflection point}\}. \tag{19}$$

Fig. 11 depicts the set $\Omega_{\mathcal{K}}$, and, for comparison, also shows the set Ω^1_{FFT}: interestingly the two sets are disjoint, showing that the two approaches target different aspects of the DIB solution, that correspond to different experimental operating conditions.

4.2. PIP in the relaxation oscillation region of the parameter space

Since the focus here is on following precisely the waveshape, we restrict the dataset for the PIP to one period (see Fig. 12). For computational convenience, we have normalized also the time axis, using the period as unit. We thus denominate $\underline{H}(C, B) = [\underline{H}_1, ..., \underline{H}_{\bar{N}}] \in \mathbb{R}^{\bar{N}}$ and $\widetilde{\underline{H}}_{exp} = [\widetilde{H}_1, ... \widetilde{H}_{\bar{N}}] \in \mathbb{R}^{\bar{N}}$ the computed and experimental chunks used for the PIP, interpolated on the same time-grid in $[0,1]$, to have the same vector size. The optimum is sought by minimizing the cost functions based on the infinity and least-squares norms given by:

$$J_\infty(C, B)_{|_{\Omega_{\mathcal{K}}}} = \|\underline{H}(C, B) - \widetilde{\underline{H}}_{exp}\|_\infty, \tag{20}$$

$$J_{2norm}(C, B)_{|_{\Omega_{\mathcal{K}}}} = \|\underline{H}(C, B) - \widetilde{\underline{H}}_{exp}\|_2^2. \tag{21}$$
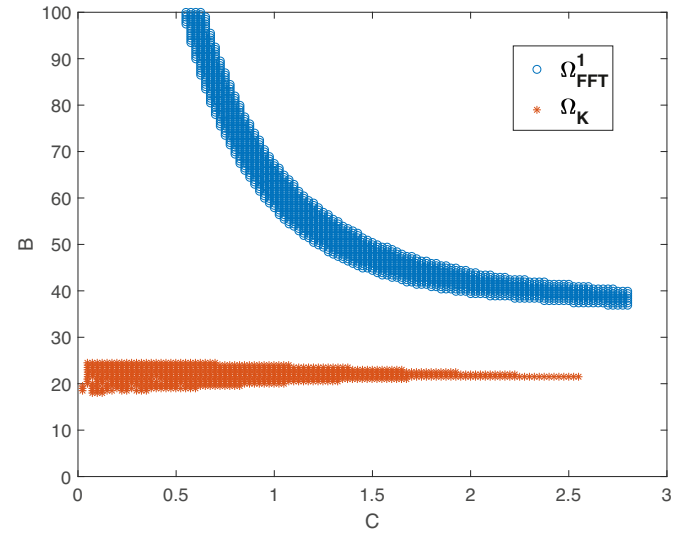

Fig. 11. Comparison of sets $\Omega_{\mathcal{K}}$ and Ω^1_{FFT} in the (C,B) parameter plane, evaluated for the dataset of Fig. 3-B.

The parametric dependence of (20) and (21) is depicted in Fig. 13 and their respective minima are: $(C_{21}, B_{21}) = (1.68, 21)$ and $(C_{22}, B_{22}) = (1.93, 22.5)$. In Panels (A)-(B) of Fig. 14 we show the respective solutions $\underline{H}(C_{21}, B_{21})$ and $\underline{H}(C_{22}, B_{22})$, that are compared with the experimental data $\widetilde{\underline{H}}_{exp}$ in Panel (C) and the corresponding absolute errors are reported in Panel (D). From Panel (C) it is possible to conclude that optimum search in the parameter subspace characterized by limit cycles with an inflection point, indeed allows to identify a couple (C, B) of parameters corresponding to a periodic solution that better approximates the complex experimental form.
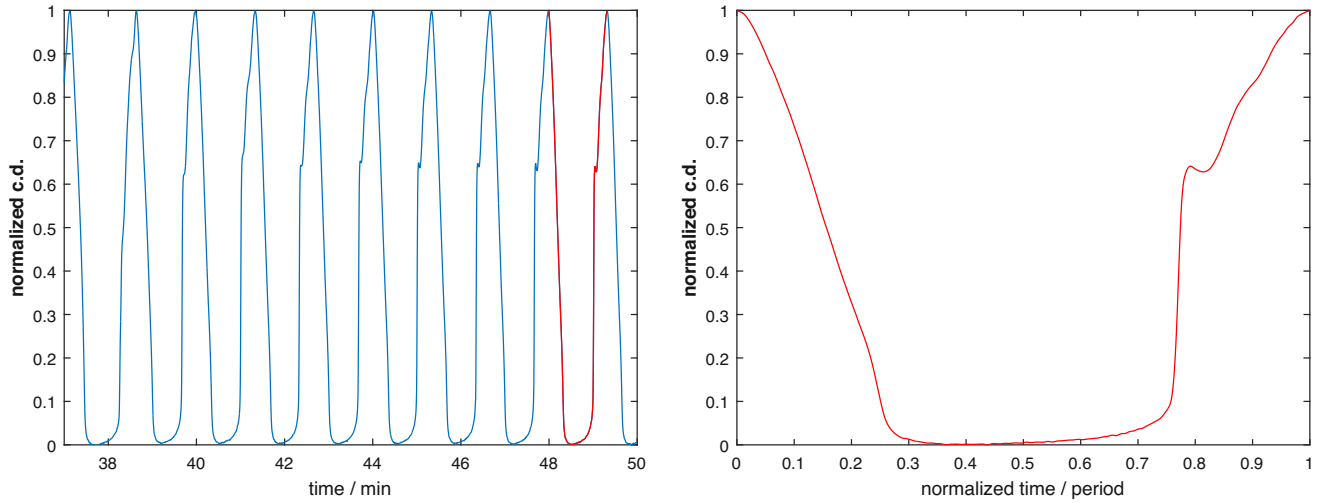
Fig. 12. The dataset $\widetilde{\underline{H}}_{exp}$ (plotted in red), extracted from the experimental time series of Fig. 3-B, employed for PIP in the relaxation oscillation region. For computational convenience, also the time axis has been normalized with respect to the period.
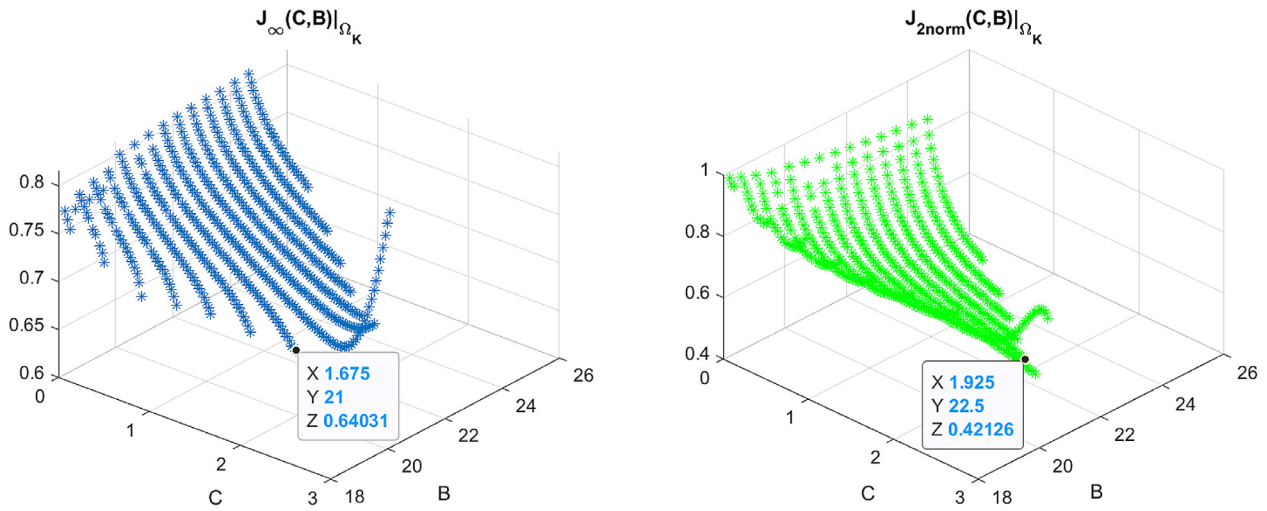

Fig. 13. The cost functions: (A) $J_\infty(C, B)|_{\Omega_{\mathcal{K}}}$ in (20) and (B) $J_{2norm}(C, B)|_{\Omega_{\mathcal{K}}}$ in (21) evaluated in correspondence of the experimental data of Fig. 12-B.

5. DIB Parameter Identification for coupled current-density and reflectivity oscillations

The physics of the DIB model crucially relies on the coupling between electrode morphology and surface chemistry. This choice of variables proved extremely successful in capturing a vast range of electrochemical spatial pattern formation processes (Bozzini et al., 2018; 2013; Lacitignola et al., 2018; 2019). So far, we have validated experimentally the DIB dynamics on the basis of exclusively morphological information (Bozzini et al., 2018; D'Autilia et al., 2017). In this section, for the first time, we propose a validation based on the experimental observation of coupled morphological (current density) and chemical (reflectivity) quantities, discussed in Section 2 and depicted in Panels (E, F) of Fig. 3. Specifically, we extracted for the analysis a representative subset of experimental data: $\widetilde{H}_1^{exp}$ for current density and $\widetilde{\Theta}_1^{exp}$ for reflectivity, that we have normalized for the reasons given in Section 3. Therefore, in this section we present the two analyses of Section 3 and 4, based on the Fourier approach and on the limite cycle approximation, respectively, for a new dataset including both $\widetilde{H}_1^{exp}$ and $\widetilde{\Theta}_1^{exp}$.

We start by defining the matrix $S_{exp}^1 \in \mathbb{R}^{N_1 \times 2}$, the columns of which contain the experimental time-series $\widetilde{H}_1^{exp}$ and $\widetilde{\Theta}_1^{exp}$. Similarly, for a given parameter couple (C, B), we have assembled in a matrix $S^1(C, B) \in \mathbb{R}^{N_1 \times 2}$ the DIB numerical solutions for both η and θ, computed by the Runge-Kutta4 method with timestep $h = 0.005$ for $t \in [0, 64]$ and initial conditions as random perturbation of the equilibrium $(\eta(0), \theta(0)) = (0, 0.5) + rand \cdot 10^{-3}$.

PIP based on Fourier analysis

Letting $\widetilde{f}_\eta$ and $\widetilde{f}_\theta$ denote the dominant frequencies of the experimental time series, inspection confirms that, as expected, $\widetilde{f}_\eta = \widetilde{f}_\theta =: \widetilde{f}_{exp}$. We then seek the parameter pair (C,B) that generates DIB solutions with the same frequency $\widetilde{f}_{exp}$. Following the approach of Section 3, we compute the subset Ω_1 of the (C, B) plane (see Fig. 15), defined as:

$$\Omega_1 = \{(C_i, B_j) \in \Omega_h \mid J_{FFT}^1(C_i, B_j) = 0\} \tag{22}$$

where:

$$J_{FFT}^1(C, B) = \frac{|f_1(C, B) - \widetilde{f}_{exp}|}{\widetilde{f}_{exp}} \tag{23}$$
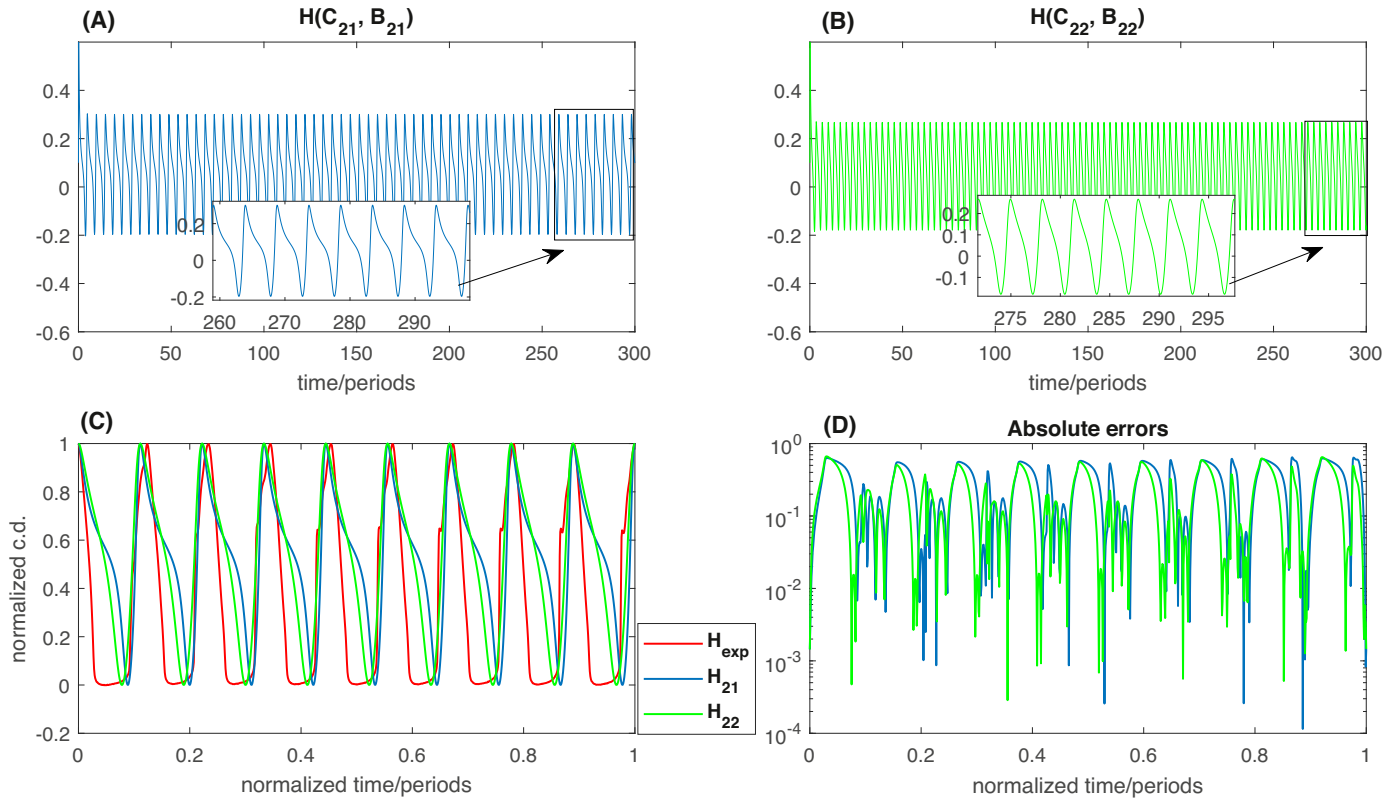
Fig. 14. (A, B) DIB solutions $\underline{H}(C_{21}, B_{21})$ and $\underline{H}(C_{22}, B_{22})$ corresponding to the minima of the cost functions reported in Fig. 13. (C, D) Comparison of $\underline{H}(C_{21}, B_{21})$ and $\underline{H}(C_{22}, B_{22})$ with the experimental data $\widetilde{\underline{H}}_{exp}$ and absolute errors.
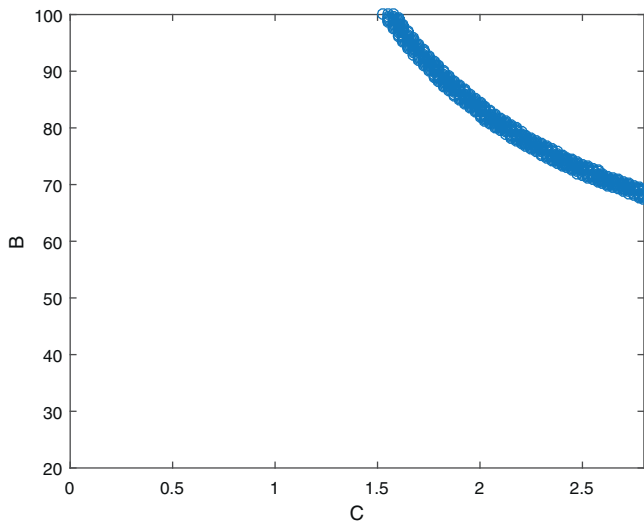

Fig. 15. The set Ω_1 of the parameter space in (22), evaluated for the datasets of Fig. 3-E and F.

being $f_1(C, B)$ the first frequency of the numerical simulations stored in the matrix $S^1(C, B)$. Optimum search is again performed by minimizing the infinity and least-squares norms given by:

$$J_\infty(C) = J_\infty(C, B)_{|\Omega_1} = \|S^1(C, B)(:) - S^1_{exp}(:)\|_\infty, \tag{24}$$

$$J_2(C) = J_{2norm}(C, B)_{|\Omega_1} = \|S^1(C, B)(:) - S^1_{exp}(:)\|_2^2. \tag{25}$$

yielding the optimal parameter couples $(C_\infty, B_\infty) = (2.78, 67.8)$ and $(C_2, B_2) = (2.80, 68.5)$. The corresponding solutions, $S^1(C_\infty, B_\infty) =$

$[\widetilde{H}_\infty; \widetilde{\Theta}_\infty]$ and $S^1(C_2, B_2) = [\widetilde{H}_2; \widetilde{\Theta}_2]$, compared with the experimental data, are plotted in Fig. 16, in the panels A and B, respectively.

Even though the exact shape of waveform cannot be approximated with the Fourier approach, nevertheless it allows to gain important insight into the relationship between operating conditions, expressed by the (C, B) couple, and the systems dynamics synthetically expressed by the dominating frequency.

PIP based on limit cycle analysis

To perform the joint limit cycle analysis on the extended dataset $S^1_{exp} \in \mathbb{R}^{N_1 \times 2}$, we built the set $\Omega_{\mathcal{K}}$ in (19) in the parameter plane (C,B) defining the relaxation oscillation region, and we minimized the cost functions (24) and (25), obtaining the pairs of parameters: $(C_{k_\infty}, B_{k_\infty}) = (2.48, 21.5)$ and $(C_{k_2}, B_{k_2}) = (2.55, 21.5)$. The optimum solutions are compared with experimental data in Fig. 17: in panels (A) and (B) in the form of time series and in panel (C) as limit cycles. Similarly to the results of Section 4, the limit cycle approach, though not allowing to capture all details of the experimental waveform, nevertheless enables an unprecedented insight into the nature of the electrochemical dynamics, correlating a specific type of oscillation with material properties and anode operating conditions.

6. Conclusions

This study is a combined mathematical and experimental analysis of the dynamics of zinc battery electrodes, polarized anodically in alkaline aqueous electrolytes. The mathematical basis of this work is the ODE version of the DIB model for phase formation and we seek regions of the parameter space that allow the ODE-DIB solutions to follow the oscillating behaviour of the electrode, found experimentally in a practically important range of operating conditions. In fact, current density oscillations result from electrical instabilities that are triggered by the onset of passivation processes, that eventually lead to electrode failure.
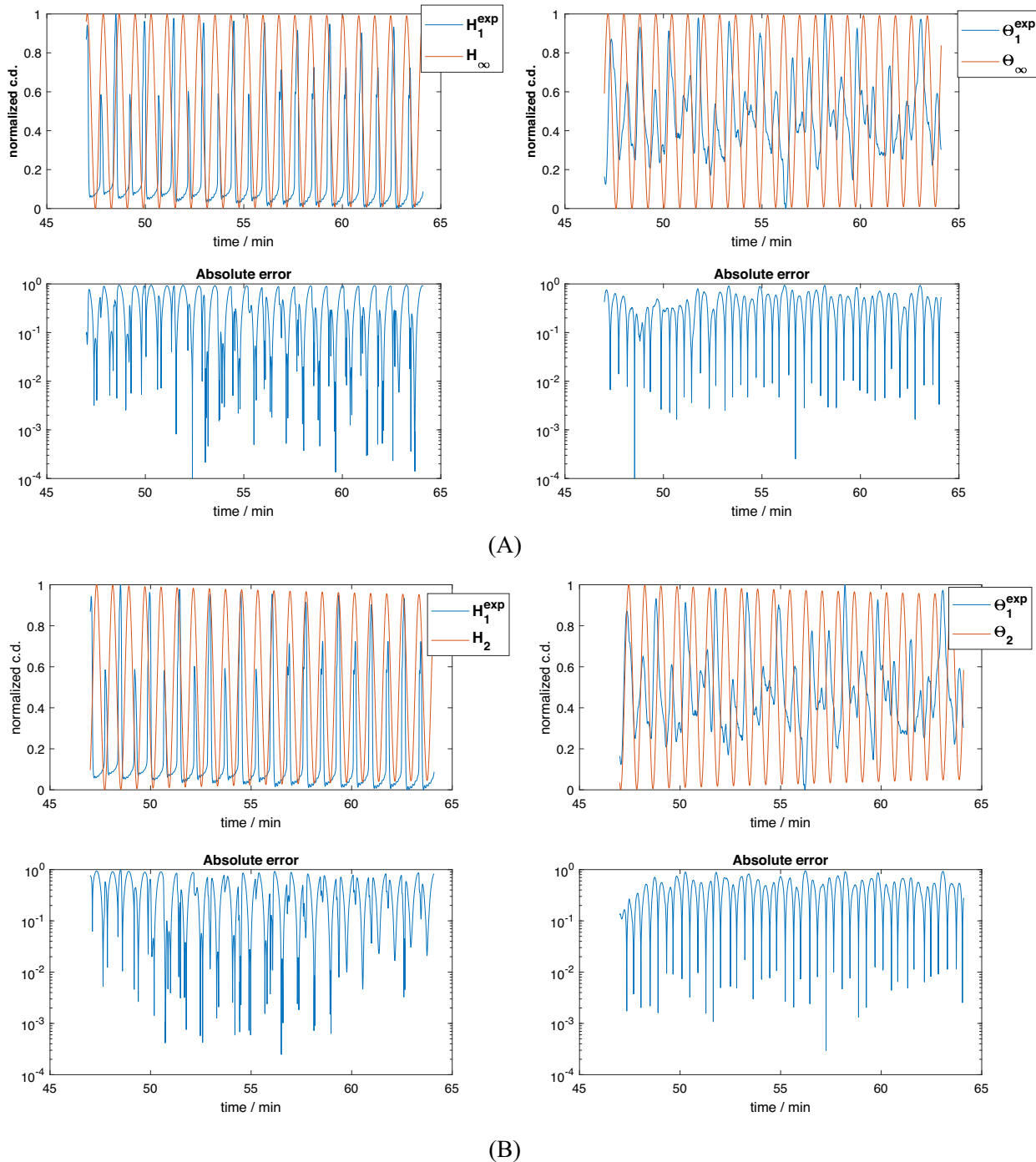
(A)

(B)

Fig. 16. Joint Fourier analysis. DIB solutions corresponding to the minima $(C_\infty, B_\infty) = (2.78, 67.8)$ and $(C_2, B_2) = (2.80, 68.5)$ of the cost functions J_∞ (Panel A, Eq. (24)) and J_2 (Panel B, Eq. (25)), evaluated on the subset of the parameter space Ω_1 in (22): comparison with experimental data and absolute errors.

Thus, physico-chemical understanding and monitoring of zinc-anode dynamics bear promise to contribute, on the one hand to the fabrication of better batteries, and, on the other hand, to improved management protocols. Moreover, here we are proposing a combined monitoring approach that features the simultaneous measurement of electrical (current density) and optical (reflectivity) quantities. The former observable, that is directly proportional to the phase formation rate, bears information on electrode morphology variations, and the latter, that is sensitive to oxi-hydroxide film formation, transduces the surface chemical composition. In addition to the electrochemical informativeness of these measurements *per se*, these two quantities closely approximate the postulated physical nature of the solutions of the DIB model: comparing this type of experimental information with results from DIB simulations thus allows to exploit the full predictive power of this model in parameter identification problems (PIP) yielding estimates that are highly informative from the physical viewpoint. In previous work in our group, we have pinpointed some aspects of the complexity of PIP with the DIB model both in the PDE (Sgura and Bozzini, 2017; Sgura et al., 2019) and in the ODE versions (D'Autilia et al., 2017). In this work we have improved and extended the portfolio of PIP methods for DIB-ODE, in
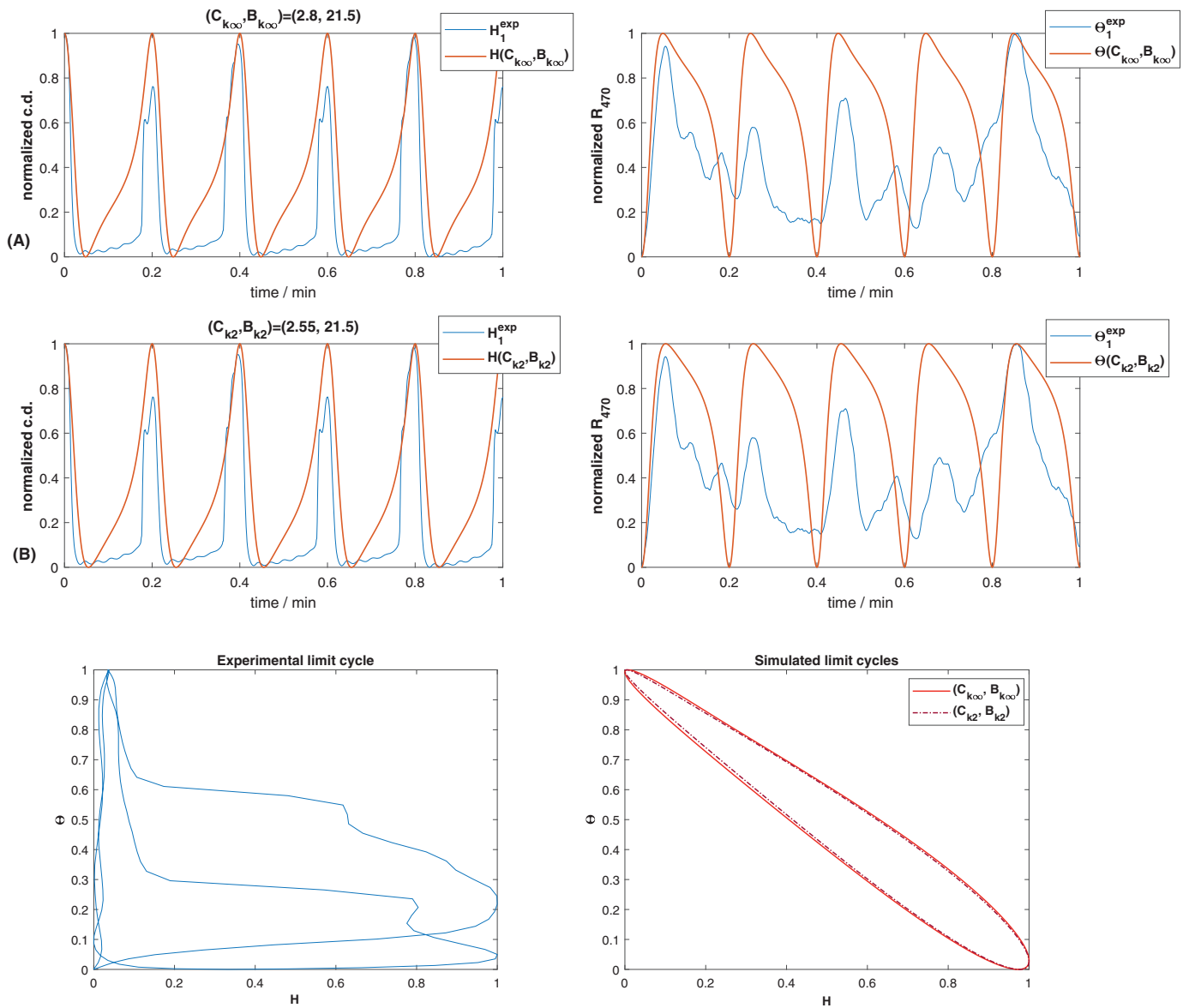
Fig. 17. Joint limit cycle analysis. DIB solutions corresponding to the minima of the cost functions (24) and (25), evaluated on the set $\Omega_{\mathcal{K}}$ of the parameter space: comparison with experimental data. (A, B) DIB solutions and experimental datasets in the form of time series; Panels (A) and (B) show solutions corresponding to $(C_{k_\infty}, B_{k_\infty})$ and (C_{k_2}, B_{k_2}), respectively. (C) same comparison in the form of limit cycles (experimental: left-hand side, numerical simulations: right-hand side).

view of efficient implementation in battery testing and control protocols. The Fourier regularization approach proposed for parameter fitting avoids ill-conditioning issues of the usual least squares approaches in case of oscillating data, and effectively identifies the dominating frequency present in quasi-periodic experimental time-series. This in practice allows to assign - on the basis of the parameter estimates - the operating conditions leading to this practically important type of dynamics. Efficiency in identification of the key aspects of the oscillating behaviour with the Fourier approach is obtained at the cost of rather a crude approximation of the oscillating waveform. This is less important in the case of quasi-harmonic oscillations, but more precision is desirable when dealing with relaxation oscillations, that are more diagnostic of operation in conditions that are liable to damage the battery. To this aim, we propose here a second PIP method for periodic DIB solutions, based on limit cycle information in the model dynamics: with this tool it is possible to identify a set of parameters that yield a reasonable matching of the experimental waveform. A notably better approximation of the waveform can only be obtained by extending the DIB model

to include a third ODE equation that would more fully account for the kinetics giving rise the relaxation processes.

Declaration of Competing Interest

The authors declare that they have no known competing financial interests or personal relationships that could have appeared to influence the work reported in this paper.

Acknowledgements

References

Arai, H., 2015. Metal storage/metal air (Zn, Fe, Al, Mg). In: Electrochemical Energy Storage for Renewable Sources and Grid Balancing P.T Moseley, J. Garche ed.s, Elsevier, p. 342s.

Blanc, L., Kundu, D., LF, N., 2020. Scientific challenges for the implementation of Zn-ion batteries. Joule 4, 1–29.

Bozzini, B., Amati, M., Dobrovolska, T., Gregoratti, L., Krastev, I., Sgura, I., Taurino, A., Kiskinova, M., 2018. Depth-dependent scanning photoelectron microspectroscopy unravels the mechanism of dynamic pattern formation in alloy electrodeposition. J. Phys. Chem. C 112, 15996–16007.

Bozzini, B., D'Autilia, M.C., Mele, C., Sgura, I., 2019. Dynamics of zinc-air battery anodes: an electrochemical and optical study complemented by mathematical modelling. Metal. Ital. 111, 33–39.

Bozzini, B., D'Urzo, L., Mele, C., 2008. Electrochemical fabrication of nano- and micrometric cu particles: in situ investigation by electroreflectance and optical second harmonic generation. Trans. Inst. Metal Finish. 86, 267–274.

Bozzini, B., Giovannelli, G., Cavallotti, P.L., 1999. An investigation into the electrodeposition of Au-Cu matrix particulate composites. J. Appl. Electrochem. 29, 685–692.

Bozzini, B., Lacitignola, D., Sgura, I., 2013. Spatio-temporal organisation in alloy electrodeposition: a morphochemical mathematical model and its experimental validation. J. Solid State Electrochem. 17, 467–479.

D'Autilia, M.C., Sgura, I., Bozzini, B., 2017. Parameter identification in ODE models with oscillatory dynamics: a Fourier regularization approach. Inverse Problems 33, 124009–124032.

Lacitignola, D., Bozzini, B., Frittelli, M., Sgura, I., 2017. Turing pattern formation on the sphere for a morphochemical reaction-diffusion model for electrodeposition. Commun. Nonlinear Sci. Numer. Simul. 48, 484–508.

Lacitignola, D., Bozzini, B., Peipmann, R., Sgura, I., 2018. Cross-diffusion effects on a morphochemical model for electrodeposition. Appl. Math. Model. 57, 492–513.

Lacitignola, D., Bozzini, B., Sgura, I., 2015. Spatio-temporal organization in a morphochemical electrodeposition model: Hopf and Turing instabilities and their interplay. Eur. J. Appl. Math. 26, 143–173.

Lacitignola, D., Sgura, I., Bozzini, B., Dobrovolska, Ts., Krastev, I., 2019. Spiral waves on the sphere for an alloy electrodeposition model. Commun. Nonlinear Sci. Numer. Simul. 79, 104930–104944.

Masri, M.N., Mohamad, A.A., 2013. Effect of adding carbon black to a porous zinc-anode in zinc-air battery. J. Electrochem. Soc. 160, 715–721.

MATLAB, 2019. R2019a. The MathWorks Inc., Natick, Massachusetts (US).

Mele, C., Bilotta, A., Bocchetta, P., Bozzini, B., 2017. Characterization of the particulate anode of a laboratory flow Zn-air fuel cell. J. Appl. Electrochem. 47, 877–888.

Mele, C., Bozzini, B., 2015. Spectroelectrochemical investigation of the anodic and cathodic behaviour of zinc in 5.3 m KoH. J. Appl. Electrochem. 45, 43–50.

Rossi, F., Mele, C., Boniardi, M., Bozzini, B., 2020. Electrodeposition of Zn from alkaline electrolytes containing quaternary ammonium salts and ionomers: the impact of cathodic-anodic cycling conditions. ChemElectroChem 7, 1752–1764.

Sgura, I., Bozzini, B., 2017. XRF map identification problems based on a PDE electrodeposition model. J. Phys. D 50, 154002–154023.

Sgura, I., Lawless, A., Bozzini, B., 2019. Parameter estimation for a morphochemical reaction-diffusion model of electrochemical pattern formation. Inverse Probl. Sci. Eng. 27, 618–647.

Shin, J., Lee, J., Park, Y., Choi, J., 2020. Aqueous zinc ion batteries: focus on zinc metal anodes. Chem. Sci. 11, 2028–2044.

Yu, Y., Xu, W., Liu, X., Lu, X., 2020. Challenges and strategies for constructing highly reversible zinc anodes in aqueous zinc-ion batteries: recent progress and future perspectives. Adv. Sustain. Syst. 2000082.

Zhu, A.L., Wilkinson, D.P., Zhang, X., Xing, Y., Rozhin, A.G., Kulinic, S.A., 2016. Zinc regeneration in rechargeable zinc-air fuel cells – a review. J. Energy Storage 8, 35–50.